# Controls on surface warming by winter Arctic moist intrusions in idealized large-eddy simulations

Antonios Dimitrelos,[a] Rodrigo Caballero[a] and Annica M.L. Ekman[a].

[a] *Department of Meteorology and Bolin Centre for Climate Research, Stockholm University, Stockholm, Sweden*

This paper is a non-peer reviewed preprint submitted to EarthArXiv

This paper is submitted to the Journal of Climate

*Corresponding author*: Antonios Dimitrelos, antonios.dimitrelos@misu.su.se

ABSTRACT

The main energy input to the polar regions in winter is the advection of warm, moist air from lower latitudes. This makes the polar climate sensitive to the temperature and moisture of extra-polar air. Here, we study this sensitivity from an air-mass transformation perspective. We perform simulations of an idealized maritime air mass brought into contact with sea ice employing a three-dimensional large-eddy simulation model coupled to a one-dimensional multilayer sea ice model. We study the response of cloud dynamics and surface warming during the air-mass transformation process to varying initial temperature and humidity conditions of the air mass. We find in all cases that a mixed-phase cloud is formed, initially near the surface but rising continuously with time. Surface warming of the sea ice is driven by downward longwave surface fluxes, which are largely controlled by the temperature and optical depth of the cloud. Cloud temperature, in turn, is robustly constrained by the initial dewpoint temperature of the air mass. Since dewpoint only depends on moisture, the overall result is that surface warming depends almost exclusively on initial humidity and is largely independent of initial temperature. We discuss possible climate implications of this result, in particular for polar amplification of surface warming and the role played by atmospheric energy transports.

## 1. Introduction

The episodic influx of warm, moist air into the Arctic during winter has a strong surface warming effect on day-to-day timescales (H.-S. Park et al. 2015, D.-S. R. Park et al. 2015, Graversen and Burtu 2019, Cardinale and Rose 2022). Around a third of the total moisture advection into the Arctic is concentrated in so-called moist intrusions—filamentary synoptic-scale structures that penetrate deep into the Arctic Ocean basin (Doyle et al. 2011, Woods et al. 2013, Liu and Barnes 2015). Elevated atmospheric temperature, humidity and cloud cover within moist intrusions generate local energy flux anomalies into the surface through increased downward longwave and turbulent fluxes (Woods and Caballero 2016, Liu et al. 2018, Sokolowsky et al. 2020, You et al. 2022) leading to local surface temperature warming of 15˚C or more over high-Arctic pack ice (Persson et al. 2017, Messori et al. 2018). The past several decades have seen an increase in the frequency of moist intrusions during winter. This trend, and related increasing trends in moisture influx and downward longwave radiation over the Arctic, can statistically explain a substantial fraction of the Arctic warming and sea-ice decline observed in that season (D.-S. R. Park et al. 2015, Woods and Caballero 2016, Gong et al. 2017, Lee et al. 2017).

This previous work suggests that moist intrusions may play a role in long-term Arctic amplification—the enhanced warming of the Arctic relative to lower latitudes that is a robust expectation for the response to global radiative forcing over the coming century (Forster et al. 2021). Conventional top-of-atmosphere (TOA) feedback analysis in climate models points to two leading causes of Arctic amplification: surface-albedo feedback associated with sea-ice retreat, and positive lapse-rate feedback associated with weaking of the climatological low-level temperature inversion (Pithan and Mauritsen 2014, Goosse et al. 2018, Hahn et al. 2021). These two feedbacks are interconnected, since Arctic lapse-rate change is partly attributable to sea-ice retreat and the resulting warming of the lower troposphere driven by increased upward surface energy fluxes (Feldl et al. 2020). Consistently, Arctic warming is observed to maximise in regions of greatest sea-ice loss during late fall and early winter, when energy absorbed by the ocean in summer is released back into the atmosphere (Screen and Simmonds 2010, Previdi et al. 2021).

However, substantial amplification occurs even in regions of the Arctic where full ice cover survives into a warmer climate, as well as over land (Taylor et al. 2022, their Fig. 10). The Antarctic continent is also robustly expected to show amplified warming in the long term (Forster et al. 2021, Hahn et al. 2020). Mechanisms other than the direct, local effect of sea-ice retreat must be invoked to explain amplification in these regions. Lapse-rate feedback in these regions is positive in fall and winter, with magnitude comparable to that in sea-ice retreat regions (Boeke et al. 2020). Water vapor and cloud feedbacks, on the other hand, are generally considered to be weak in the Arctic (Pithan and Mauritsen 2014, Goosse et al. 2018, Hahn et al. 2021, Middlemas et al. 2020). Weak cloud feedbacks may be due to underrepresentation of Arctic cloud liquid water content, a bias common to many climate models (Pithan et al. 2014, 2016; Middlemas et al. 2020) and also cloud-resolving models (Klein et al. 2009).

Advective transport processes are likely to be particularly important in warming polar pack-ice and continental regions. Arctic amplification is partly due to the asymmetric impact of advective exchange between polar and lower latitudes (Taylor et al. 2022): the Arctic responds strongly to midlatitude radiative forcing, while the midlatitudes respond negligibly to Arctic forcing (Stuecker et al. 2018, Semmler et al. 2020). Global forcing therefore has a double—local and remote—impact on the Arctic. Midlatitude forcing can only make itself felt in the Arctic through changes in advective transport. Climate models subject to global forcing robustly show increased latent heat transport to the Arctic, but offset by a similar-sized decrease in dry static energy transport. This compensation results in small or even negative change in total atmospheric transport (Hwang et al. 2011, Hahn et al. 2021). The strong Arctic response to midlatitude forcing can be reconciled with small change in total energy transport if the Arctic is much more sensitive to latent than to dry energy transport (Graversen and Burtu 2016, Yoshimori et al. 2017, Graversen and Langen 2019). However, the precise mechanisms explaining this different sensitivity remain unclear.

Moist intrusions are sites of concentrated moisture and cloudiness anomalies tied to transport from lower latitudes. A deeper mechanistic understanding of the processes occurring within moist intrusions may therefore yield insight into the role played by transport in Arctic amplification. Here, we study the air-mass transformation process within idealized moist intrusions using a column-model framework. The column is initialized with temperature and moisture profiles representative of subpolar marine air and allowed to evolve freely, aiming to capture the Lagrangian air-mass transformation process as the column is advected into the Arctic and cools by longwave radiative emission and interaction with a cold surface. Our study extends a long tradition of such Arctic column-model work (Wexler 1936, Herman and Goody 1976, Curry 1983, Cronin and Tziperman 2015, Pithan et al. 2014, 2016). Differently from previous work, we employ a fully 3-dimensional large-eddy simulation (LES) model to capture cloud and turbulence dynamics with as much realism as possible.

The LES model is coupled at its bottom boundary to a simple thermodynamic sea ice model which assumes complete and uniform ice cover (see Section 2). Our results can therefore say nothing about the potential role of moist intrusions in driving reduced sea-ice cover, and they miss the important role of surface fluxes through leads and newly-open water in generating Arctic clouds (Kay and Gettelman 2009). Instead, the results are relevant to regions with persistent dense sea-ice cover, and to some extent also land, which like sea ice has low heat capacity and limited surface fluxes. As noted above, these regions also experience amplified warming. We also neglect solar radiation, so our results are most relevant for polar winter.

We focus on the question of how the initial temperature and humidity of the air column separately affect the subsequent cloud evolution and surface impacts during the air-mass transformation process. One might a priori expect that, for a given humidity, an initially warmer air mass would produce greater surface warming—both by producing warmer clouds with greater surface radiative impact, and by enhancing sensible heat flux into the ice. Our key result, presented in Section 3, is that this is not the case: initial temperature makes little difference to surface warming. Instead, surface warming is controlled mostly by initial humidity. As discussed in Sections 4 and 5, the main reason for this behavior is that cloud and sub-cloud temperatures are constrained by the air mass's initial dewpoint temperature, which depends only on its humidity. In Section 6 we summarize our conclusions and discuss their potential implications for Arctic climate and amplification.

## 2. Methods

*a. Large-eddy simulation model*

We employ the MISU-MIT Cloud and Aerosol model (MIMICA, Savre et al. 2014), a three-dimensional LES model using a 1.5 order subgrid-scale turbulence closure scheme. The surface turbulent fluxes are calculated using Monin-Obukhov similarity theory (Garrat 1994). The model includes a two-moment bulk microphysics scheme, where prognostic equations for the mass mixing ratio and number concentration of hydrometeors are solved. Five types of hydrometeors are considered: cloud droplets, raindrops, pristine ice crystals, snow, and graupel. In this study, the snow and graupel categories are excluded, since we found that aggregation, riming and accretion did not affect the results. The size distributions of the hydrometeors are prescribed by gamma functions (Savre et al. 2014) and their terminal fall speeds are described by simple power laws (Pruppacher and Klett 1997). The ice crystal habit was defined to be plate, in agreement with the cloud layer temperatures obtained during the simulations. The warm microphysics interactions are parameterized according to Seifert and Beheng (2001) and the supersaturation is explicitly calculated at every model time step (Morrison and Grabowski, 2008). The number of activated cloud condensation nuclei (CCN) is calculated as in Khvorostyanov and Curry (2005) and all CCN are assumed to consist of ammonium sulfate. The ice crystal number concentration (ICNC) is relaxed towards a fixed background value according to Morrison et al. (2011). A multiband 2-4 stream radiative solver is used to calculate the radiative flux densities (Fu and Liou 1993). The radiative solver takes into account the mixing ratio of all hydrometeor types. Prescribed vertical profiles of parameters that describe the atmosphere are used to calculate radiative fluxes from the domain top to the top of the atmosphere. Lateral boundary conditions are periodic and a sponge layer is applied at the domain top to damp any gravity waves. For the simulations in this study, the length and width of the domain is set to 6 km, while its vertical extent is 4 km. The horizontal grid spacing is set to 62.5 m, and the vertical grid is split into two zones. The layer from the surface up to 2.5 km has a resolution of 15 m. The upper part of the domain has a higher resolution of 7.5 m. This grid division prevents numerical instabilities originating from gravity waves formed at cloud top when the cloud dissipates, which occurs at heights above 2.5 km.

*b. Sea ice model*

A 1-dimensional thermodynamic sea ice model was developed and coupled to MIMICA in order to study the surface and subsurface warming effect of the clouds. The model is an upgraded version of that used in Dimitrelos et al. (2020), which was a one-layer slab sea ice model. Here, the sea ice model includes four layers to better represent heat conduction within the sea ice and energy exchange with the atmosphere. The surface layer is assumed to be snow while the underlying layers are ice of different characteristics. A schematic of the model is presented in Figure 1. The model solves energy balance equations at the layer interfaces and heat conduction within the layers. A detailed description of the model equations and parameter values is provided in the Appendix.

The atmosphere and sea ice interact through the surface energy balance equation

$$F_{LWd} - F_{LWu} + F_{SH} + F_{LH} + F_C = 0, \qquad (1)$$

where $F_{LWd}$ and $F_{LWu}$ are surface downward and upward longwave fluxes respectively, $F_{SH}$ and $F_{LH}$ are turbulent sensible and latent heat fluxes, described through a bulk aerodynamic approximation (see Appendix) and $F_C$ is the surface conductive flux, which depends on the temperature difference between the surface and the underlying snow layer. Horizontal-mean values of near-surface air properties and radiative fluxes are used as fluxes into the sea ice model, while the surface temperature and upward fluxes computed by the sea ice model are provided as input to the atmospheric model uniformly at all grid points. Solar radiative fluxes are absent as our simulations target polar night.

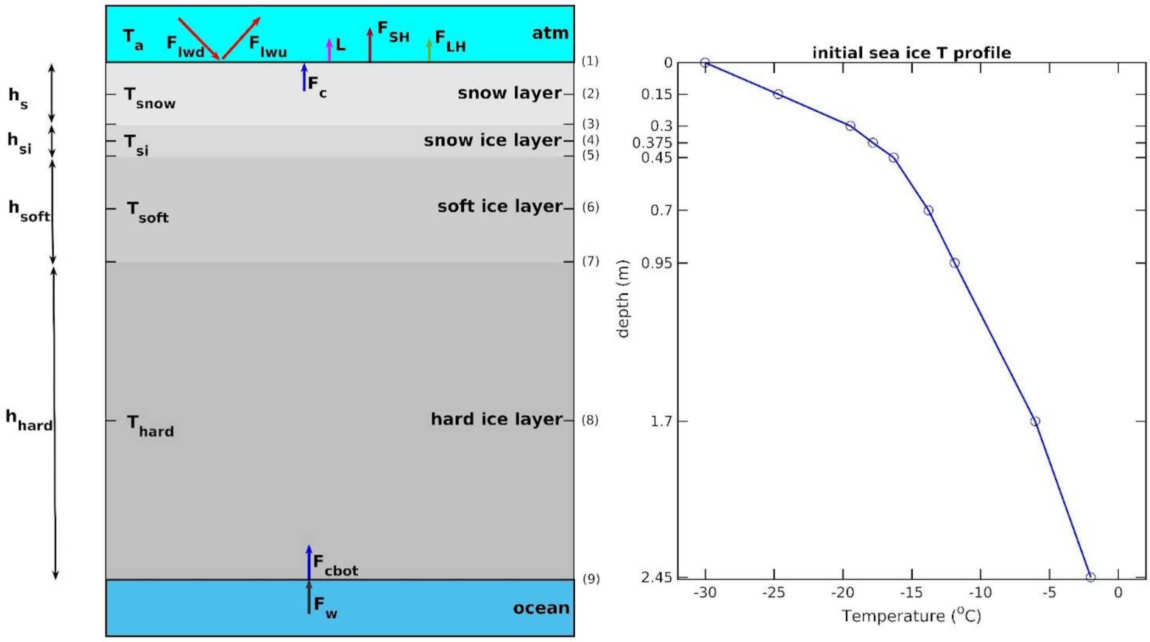


Fig. 1. (Left) Schematic of the sea ice model. Symbol definitions and a detailed description of the model is provided in the Appendix. (Right) Initial temperature profile in the sea ice model.

An initial sea ice temperature profile is defined through an offline simulation of the sea ice model with $F_{LWd}$ fixed at 170 W m$^{-2}$ (matching observed clear-sky values in the high Arctic, Persson et al. 2017) while the air temperature at 10 m altitude is set to be 0.5˚C warmer than the surface temperature, yielding surface turbulent fluxes ~1 W m$^{-2}$. The sea ice model is run under these conditions until all layers reach the steady-state temperature profile shown in Figure 1b. In this state, surface temperature is –30˚C, net longwave radiative flux $F_{LWd} - F_{LWu}$ = –12 W m$^{-2}$ while $F_C$ = 11 W m$^{-2}$.

*c. Simulation setup*

Each simulation is initialized with the atmospheric temperature and humidity profiles specified below, intended to represent the typical conditions of subpolar marine air. The sea-ice model is initialized with temperature profile shown in Figure 1b, meant to represent climatological conditions for the winter high Arctic. No external lateral boundary fluxes are imposed (the flow is re-entering at the lateral boundaries). There are limitations to the realism of this approach. An advected air column will in reality continuously encounter unperturbed sea ice, rather than always interacting with the same sea ice as in our simulations. Also, a real air column will generally be deformed by large-scale wind shear rather than conserve its vertical coherence. Nonetheless, we employ this approach in the interest of simplicity and consistency with previous work.

In all simulations, the initial atmospheric temperature profile takes the form $T = T_0 - \Gamma z$, where $z$ is height and the lapse rate $\Gamma$ = 8˚C km$^{-1}$ in all cases (examples of this structure are shown in Figure 5d-f, lines marked with a 0). The relative humidity profile takes the same form, RH = RH$_0 - \Gamma_{RH} z$, with $\Gamma_{RH}$ =15% km$^{-1}$. The simulations are distinguished only by the initial surface values $T_0$ and RH$_0$. We perform simulations with all combinations of three $T_0$ values (0, 5 and 10˚C) and three RH$_0$ values (70, 80 and 90%), for a total of nine simulations. These values are chosen to roughly capture typical subpolar maritime conditions in the modern (Ali and Pithan, 2020) and warmer future climates. To identify these simulations we use the notation T$x$RH$y$, where $x$ represents the $T_0$ value and $y$ represent the RH$_0$ value, so e.g. our coldest and driest simulation, with $T_0$ = 0˚C and RH$_0$ = 70% (to be used as a reference case in Section 3) is referred to as T0RH70.

A further set of six simulations was designed to test the sensitivity to changing initial *specific* humidity at fixed initial temperature and vice-versa. Three of these simulations (denoted T0Lo, T5Lo and T10Lo) have initial $T_0$ = 0, 5 and 10˚C respectively but all have the same initial specific humidity profile as in T0RH90. The other three (T0Hi, T5Hi and T10Hi) all have the higher initial specific humidity profile of T5RH90. Note that T0Lo is actually the same as T0RH90 while T5Hi is the same as T5RH90; also, the T0Hi simulation was omitted as its initial temperature and humidity values imply supersaturation. We thus have a total of 12 distinct simulations.

All simulations are initially cloud-free and assume a fixed number concentration of CCN (30 cm$^{-3}$) and ICNC (1 liter$^{-1}$). These values are realistic for the winter Arctic (Mauritsen et al. 2011; Wendisch et al., 2019). An initial vertically uniform mean horizontal wind of 5 m s$^{-1}$ is applied to all experiments, and the winds are nudged to their initial value throughout the simulation. All simulations assume zero divergence and large-scale subsidence. Shortwave radiation is zero in all cases as we are assuming polar night. Each simulation is run for 5 days, the typical observed transit time of moist intrusions across the Arctic basin (Woods and Caballero 2017).

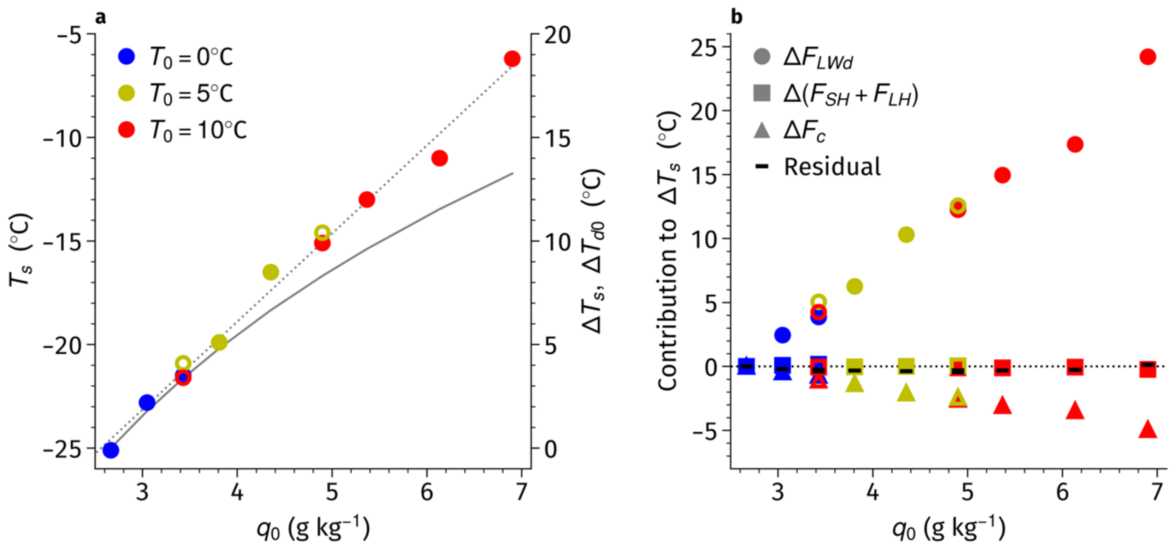


Fig. 2. (a) Time-mean ice-surface temperature $T_s$ (left axis) as a function of initial surface specific humidity $q_0$ for all simulations. Dotted line shows the linear regression of $T_s$ against $q_0$. The right axis shows $\Delta T_s$, the change in $T_s$ from its value in the reference case T0RH70. Solid line (right axis) shows $\Delta T_{d0}$, the change in initial surface dewpoint $T_{d0}$ from its value in the reference case.(b) Decomposition of the surface temperature response into contributions from downward longwave flux (circles), turbulent fluxes (squares) and conductive flux (triangles), see Equation (2) in text. All values are plotted as differences from the reference case T0RH70. The residual (thick black dashes) is the difference between $\Delta T_s$ derived using (2) and the actual $\Delta T_s$ in the simulations. Colors indicate the initial air surface temperature $T_0$ (see legend in panel a). Open symbols indicate the T5Lo, T5Hi and T10Lo cases.

## 3. Surface warming response

Our simulations aim to capture the situation where a moist intrusion carrying subpolar marine air reaches unperturbed sea ice that is at the typical climatological temperature of pack ice in the winter high Arctic. Figure 2a plots the time-mean ice-surface temperature $T_s$ over the 5-day duration of each simulation as a function of the initial surface specific humidity $q_0$. Depending on the initial atmospheric conditions, the surface warms by 5–25˚C above its initial temperature of –30˚C over the course of the air-mass transformation process. This magnitude of warming is consistent with surface temperature anomalies typically observed during moist intrusion events in the wintertime high Arctic (Woods and Caballero 2016, Messori et al. 2018).

The results in Figure 2a show that increasing initial humidity drives increased surface warming, following an approximately linear relationship (dotted line). We also note that simulations with the same initial humidity but different initial temperatures have very similar surface warming: specifically, T0Lo, T5Lo, and T10Lo (which all have initial $q_0$ of around 3.5 g kg$^{-1}$) all result in $T_s$ of about –21˚C, while T5Hi and T10Hi ($q_0 \approx 5$ g kg$^{-1}$) both yield $T_s$ of around –15˚C. The surface temperature response—at least in the time-mean—is therefore controlled almost entirely by the initial specific humidity, with initial temperature playing a negligible role. Put another way, two air-mass transformation processes starting with the same relative humidity but different temperatures have different surface impacts only by virtue of their different specific humidity, not directly because of their different temperature.

To determine the proximate causes for the surface temperature response, we decompose it into contributions from different surface flux terms by linearising the surface energy balance Equation (1) around a reference surface temperature (Lee et al. 2017):

$$\Delta T_s \approx (\Delta F_{LWd} + \Delta F_{SH} + \Delta F_{LH} + \Delta F_C)/4\epsilon\sigma T_s^3, \quad (2)$$

where $\Delta T_s$ is the difference in time-mean $T_s$ between a given simulation and a reference simulation (taken as T0RH70, our coldest and driest case). Differences in downward longwave radiative flux $\Delta F_{LWd}$, turbulent sensible and latent heat fluxes $\Delta F_{SH}$ and $\Delta F_{LH}$, and conductive heat flux $\Delta F_C$ at the surface (again time-averaged over the first 5 days of each simulation) are computed in a similar manner. Figure 2b shows the terms on the r.h.s. of (2) for each simulation. The residual in (2), i.e. the difference between the sum of the four terms on the r.h.s. and the model-produced $\Delta T_s$ is very small, implying that (2) provides an adequate approximation.

Figure 2b shows that the longwave and conductive terms scale roughly linearly with initial humidity, while the turbulent flux terms change little across the simulations. The only positive term is downward longwave radiation, which is therefore the sole driver of increased surface warming with increasing humidity, and is only partly offset by the increasingly negative conductive term, i.e. by increased cooling of the surface through heat transfer into the underlying snow and ice. The dominant role of downward longwave radiation in driving surface temperature change is consistent with observational work over pack ice in winter (e.g. Lee et al. 2017). Cases with the same initial specific humidity show very similar values of $\Delta F_{LWd}$, $\Delta F_{SH}$ and $\Delta F_C$, so initial humidity is the dominant control not just on the overall surface temperature response, but on individual surface energy budget terms as well.

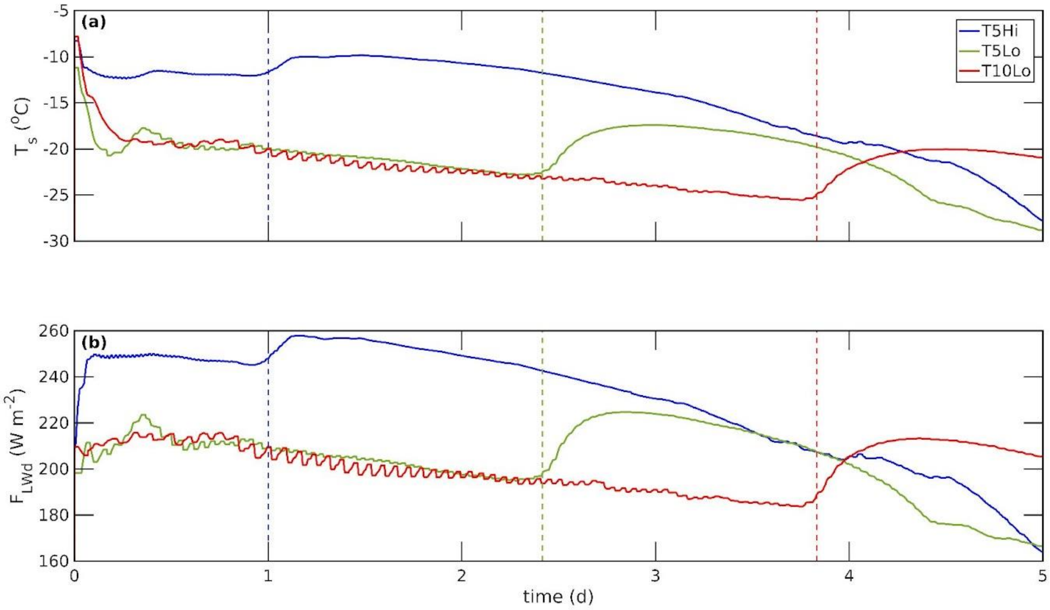


Fig. 3. Time evolution of horizontally-averaged (a) surface temperature $T_s$ and (b) surface downward longwave flux $F_{LWd}$ for T5Hi (blue lines), T5Lo (green) and T10Lo (red). Vertical dashed lines in corresponding colors mark the transition from the stable to the convective regime.

## 4. Cloud dynamics and the role of initial dewpoint temperature

To better understand the results of the previous section, we select three specific simulations for closer examination: two with equal initial temperature but different initial humidity (T5Lo and T5Hi), and another, T10Lo, with the same initial humidity as T5Lo but higher initial temperature. These simulations are indicated by open symbols in Figure 2.

Figure 3 shows the time evolution of surface temperature and downward longwave flux in the three simulations. Comparing Figures 3a and 3b, it is clear that surface temperature closely tracks the downward longwave flux not just in the time mean, as shown in the previous section, but at every instant. This is because of the low effective heat capacity of the surface, which allows surface temperature to respond very quickly to changes in surface energy fluxes, a point we return to in Section 5. Since we expect downward longwave radiation to be heavily influenced by the presence and nature of clouds in the air column, we devote the rest of this section to an analysis of cloud evolution during the simulations. Note for example that surface temperatures show sudden upward jumps at specific stages during each simulation (dashed lines in Figure 3); these correspond to cloud regime transitions discussed below.

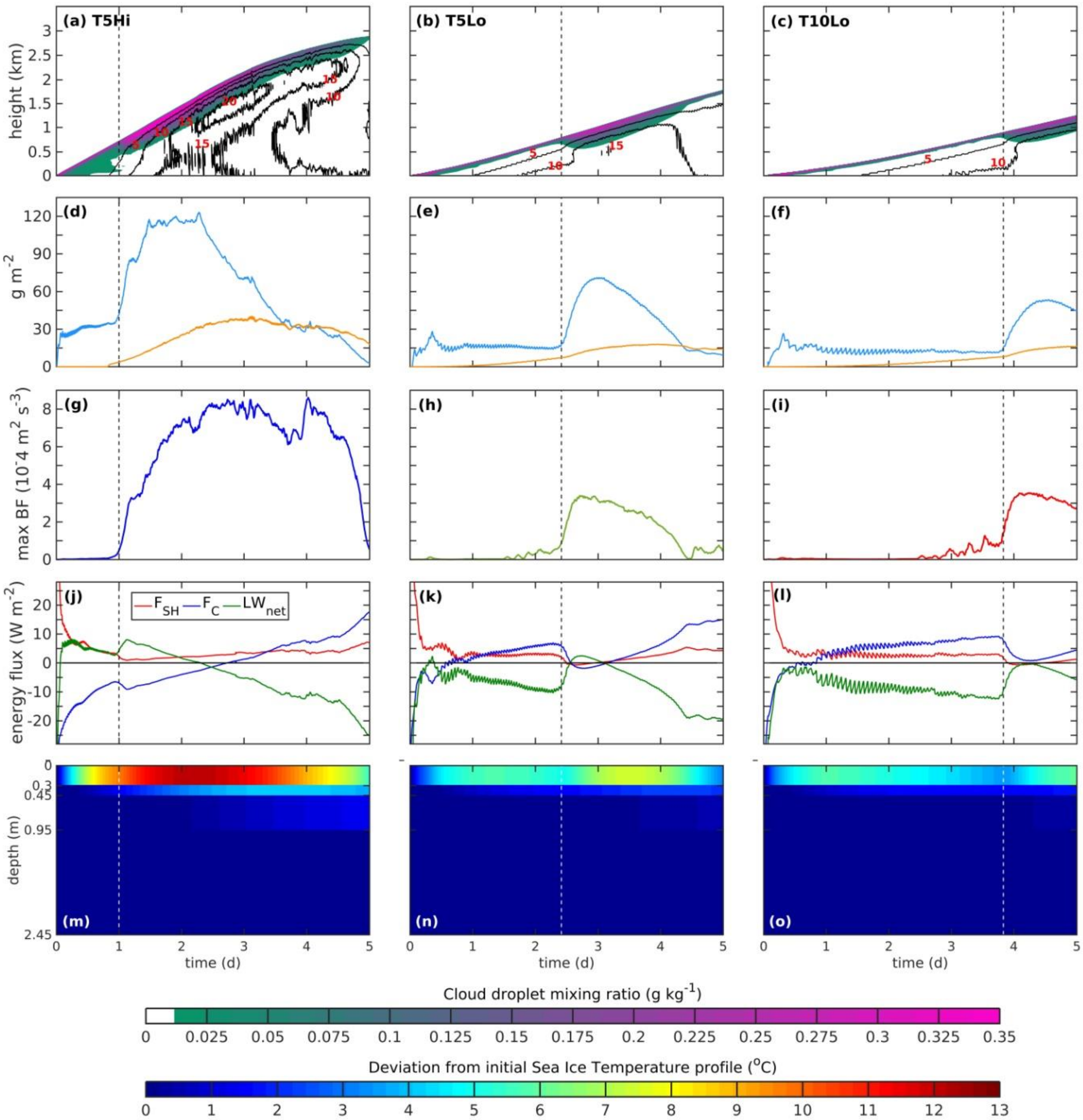


Fig. 4. Time evolution of horizontal-mean (a-c) cloud liquid water mixing ratio (shading) and ice crystal mixing ratio (contours at intervals of 5 mg $kg^{-1}$); (d-f) liquid water path (blue line) and ice water path (yellow); (g-i) maximum value of horizontally-averaged turbulent buoyancy flux; (j-l) surface net longwave flux (green lines), sensible heat flux (red) and conductive flux (blue); (m-o) mid-layer temperatures in the ice model, shown as the difference from the initial temperature profile (Figure 1b). Dashed vertical lines in each panel denote the transition from the stable to the convective regime. Left, middle and right columns show results for T5Hi, T5Lo and T10Lo respectively.

*a. Cloud regimes*

Figure 4a-c presents the time evolution of cloud condensate in the three simulations. All three exhibit cloud tops initially near ground level but steadily rising throughout the 5 day period. This behavior is common to all simulations conducted in the present study. Note that the cloud elevates most rapidly in the moister case T5Hi, while among the two drier cases it rises fastest in the initially colder one (T5Lo). We examine the reasons for these different elevation rates below.

Another feature common to all three cases is that buoyancy-driven turbulence (as measured by the maximum positive turbulent buoyancy flux, Figure 4g-i) is initially near zero, transitioning sharply to larger values only some time into the simulations. We can therefore distinguish two distinct stages of cloud evolution: an initial stable, non-convective regime, followed by a turbulent convective regime. For reference, dashed lines in Figure 3 show the approximate time at which this transition occurs in each simulation. In the late stages of the simulations, the buoyancy flux decreases to near-zero once again as the cloud dissipates, and we can distinguish a third, decay stage (visible for T5Hi and T5Lo, but a longer simulation would be required to capture it in T10Lo). We focus below on the stable and convective regimes.

Profiles of ice-liquid-water potential temperature at different times in the simulations (Figure 5a-c) show that the entire column is indeed statically stable during the stable regime, but in the convective regime it becomes neutrally stable within a layer immediately below the cloud, remaining strongly stable near the surface. The convective regime profiles are consistent with vigorous convection driven by cloud-top radiative cooling and mixing below the cloud, yielding the neutrally-stable profile there, but convection does not penetrate all the way to the ground because of strong near-surface stability. We can thus characterize the convective regime as a stratocumulus-topped convective layer overlying a decoupled surface layer, a regime well known from previous observational and modeling studies of polar clouds (Shupe et al. 2013; Solomon et al. 2011; Svensson and Mauritsen 2020). The stable state with a fog or thin stratus cloud is less well characterized observationally, though fogs or very low, thin stratus are often observed near the sea ice margin (Sotiropoulou et al. 2016).

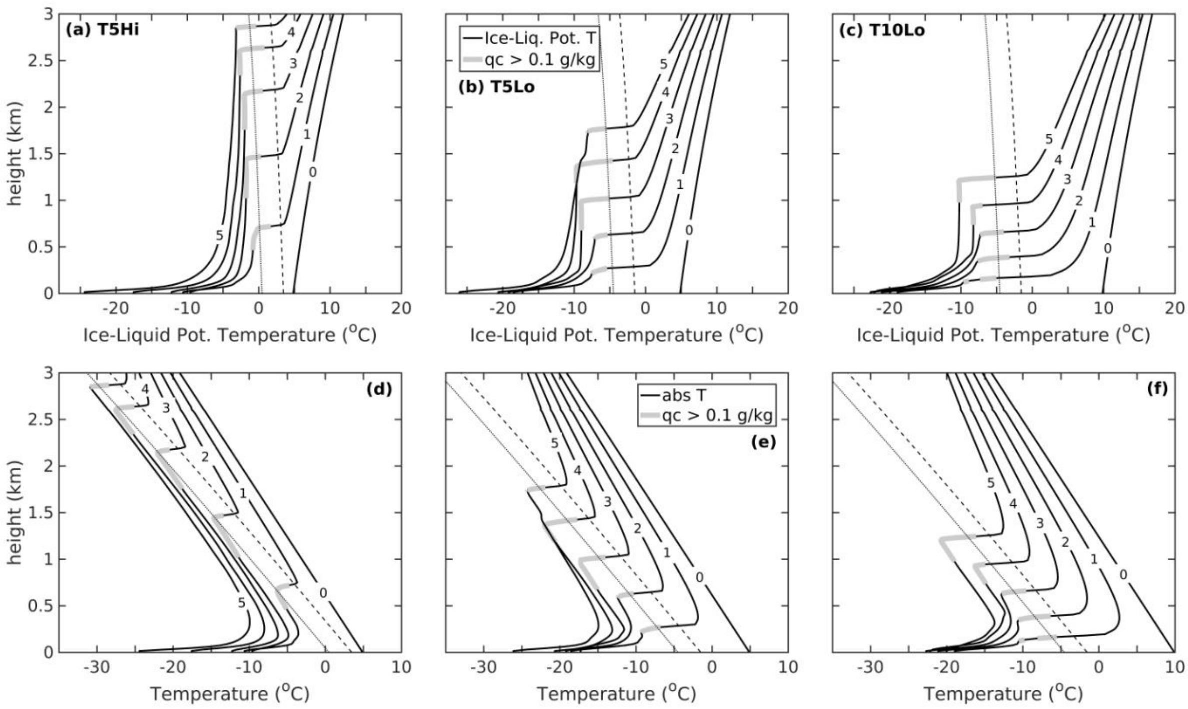


Fig. 5. Profiles of horizontal-mean ice-liquid potential temperature (top row) and absolute temperature (bottom) at selected times; numbers within each line show time in days from the start of each simulation. Gray shading indicates cloud (liquid water mixing ratio larger than 0.1 g kg$^{-1}$). Thin dashed lines show (a-c) initial dewpoint ice-liquid potential temperature and (d-f) initial dewpoint temperature. Thin solid lines show the corresponding profile minus 3˚C. Left, middle and right columns show results for T5Hi, T5Lo and T10Lo respectively.

### *b. The stable regime*

In the stable (stratus) regime cloud-top lifting is radiatively driven (Herman and Goody 1976). In the initial clear-sky state, atmospheric radiative and sensible cooling maximizes near the surface, and near-surface air cools rapidly until its temperature drops below the dewpoint. A cloud (or fog) then forms and further cooling is slowed by latent heat release. This cloudy layer becomes opaque to longwave radiation, shifting the radiative cooling peak upward to the interface with the overlying clear air. The clear-air layer just above the cloud top then cools below its dewpoint and becomes cloudy; once sufficient condensate has formed to render it opaque, radiative cooling again shifts upwards and the whole process repeats in the layer above. As a result, cloud top in the stable regime rises in a layer-by-layer process controlled only by the local radiative cooling and latent heating within each layer.

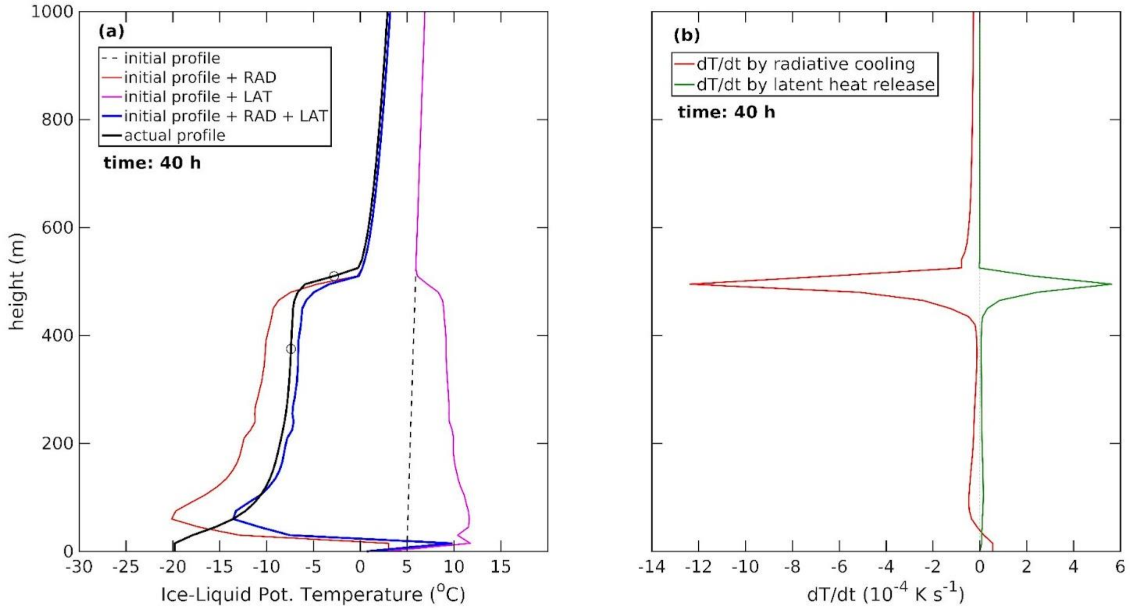


Fig. 6. Example of the roles played by radiative cooling and condensational heating in determining the atmospheric temperature profile. (a) Horizontal-mean ice-liquid potential temperature profile after 40 hours in the T5Lo simulation (black solid line), compared with the profile that would result if radiative cooling had acted alone (red line), if latent heating had acted alone (magenta line), and if the sum of radiative and latent heating had acted alone (blue line). Thin dashed line displays the initial ice-liquid potential temperature. Circles mark cloud top and base. (b) Instantaneous horizontal-mean radiative cooling rate (red line) and latent heating rate (green line) at $t$ = 40 hours in the T5Lo simulation.

Support for this conceptual picture comes from Figure 6a, which shows the time-integrated radiative cooling and latent heating after 40 hours of the T5Lo simulation. The combined effect of these two tendencies yields a temperature profile that closely matches the actual simulated profile except near the surface. This close match implies that the sub-cloud temperature structure in the stable regime is determined almost entirely by local radiation and latent heat release, with no role for turbulent mixing except near the surface, where mechanical turbulence generates sensible heat flux from the atmosphere toward the colder surface below.

The simulations all exhibit substantial drizzle at peak rates of over 1 mm day$^{-1}$ during the stable regime, along with some ice precipitation, which rapidly deplete cloud condensate and dissipate the cloud except in the thin layer where cloud formation is actively occurring. The resulting cloud is thus thin, filling a layer of only ~100 m thickness (Fig. 4a-c) with a liquid water path of 20–30 g m$^{-2}$ (Fig. 4d-f). A sensitivity study in which drizzle is artificially suppressed (Dimitrelos et al. 2020) shows the entire layer from surface to cloud top fills with cloud condensate, driving higher surface temperature during the stable regime. Arctic low stratus clouds are commonly observed to produce supercooled drizzle, at least in spring and summer (Lawson et al. 2001, Tjernström 2007). We are not aware of observed drizzle rates which could help constrain this aspect of our simulations, however.

The picture outlined above implies that cloud temperature is, to a first approximation, determined by the dewpoint temperature of the initial maritime air mass. Both radiative cooling and latent heating rates drop to near-zero below the cloud, as shown in Figure 6b. The temperature in a given layer will therefore remain close to its value at the time of cloud formation, even after the cloud has shifted upward. The entire sub-cloud temperature structure—except near the surface, where cooling by sensible heat flux divergence is important—remains close to the original dewpoint temperature profile. This fact is highlighted in Fig. 5d-f, where dashed lines show the initial dewpoint temperature and thin solid lines show a temperature profile 3˚C colder than the dewpoint; the latter gives a reasonable match to cloud temperature throughout the simulation in all cases.

We can therefore interpret the air-mass transformation process during the stable regime simply as a readjustment of the sub-cloud temperature to a profile matching the initial dewpoint profile but shifted a few degrees colder. The initial temperature profile is in this sense irrelevant, since the dewpoint is controlled only by initial humidity. This helps explain why the surface temperature impact in our simulations (Figure 2) is controlled only by initial humidity while initial temperature plays a marginal role.

Initial temperature does play a role however in controlling the rate of ascent of the cloud: for a given initial humidity, a warmer initial temperature will need to cool for a longer time to reach the dewpoint; hence the slower rate of ascent in the T10Lo simulation than in T5Lo. Initial temperature also controls the strength of the cloud-top temperature inversion: for a given initial humidity, an initially warmer profile will generate a stronger inversion, since the inversion strength is approximately the difference between temperature and dewpoint.

*c. The convective regime*

The initial dewpoint temperature profiles are slightly unstable at all heights, and increasingly so at higher levels (Figure 5a-c). Cooling by sensible heat transfer to the surface keeps the temperature profiles stable at lower levels, so the cloud must rise to some height (around 750 m in all three cases) before convection can set in. As the cloud enters the convective (stratocumulus) regime it continues to rise, at a rate now set by cloud-top turbulent entrainment since there is no large-scale subsidence in these simulations (Mellado 2017). The cloud deepens substantially (Figure 4a-c) and liquid water path rises sharply to peak values in the range 60–120 g $m^{-2}$ (Figure 4d-f), while cloud liquid content reaches ~0.35 g $kg^{-1}$ (Figure 4a-c); such values are consistent with observations in the high Arctic (Verlinde et al. 2007; Persson et al. 2017; Silber et al. 2021; Shupe et al. 2008). As a result, cloud base becomes lower and therefore warmer, while the cloud itself becomes optically thicker. Both these effects help explain the sudden upward jump in downward longwave radiation seen in Figure 3b as the cloud transitions from the stable to the convective regime.

Drizzle ceases in the convective regime and ice precipitation takes over as the main cloud sink. Accumulated over the entire cloud life cycle, ice precipitation is in fact the dominant cloud sink, as expected for Arctic clouds (Morrison et al. 2012). Ice water content of up to ~0.02 g $kg^{-1}$ can be seen within and below the liquid cloud layer (Figure 4a-c), consistent with observed values (Shupe et al. 2008). Our simulations exclude ice aggregation into graupel or snow, so all ice precipitation occurs as a result of ice particle growth by vapor deposition to sufficient size to settle out of the cloud. A sensitivity study in which aggregation is enabled shows that the greater particle sizes lead to enhanced settling rates, but this does not strongly affect the rate of primary ice particle production from supercooled liquid, so that the depletion rate of cloud liquid water (and therefore the liquid water path) is not strongly affected.

Once in the convective regime, entrainment and mixing provide an additional source of energy to the cloud layer. Cloud temperature could therefore depart substantially from its previous stable-state value, which as argued above is set by the initial air mass dewpoint. It turns out however that the departure is small—a modest cooling of ~2˚C (Figure 5a-c; note that the transition from stable to convective regimes occurs after 1, 2.4 and 3.8 days for T5Hi, T5Lo and T10Lo respectively). As a result, cloud temperature is still to a first approximation controlled by initial dewpoint even in the convective regime.

This behavior can be understood by considering the bulk energetics of the well-mixed sub-cloud layer (Stevens 2006):

$$\frac{ds}{dt} = \frac{E\Delta s - \Delta F_{rad} - F_b}{h}, \tag{3}$$

where $s$ is the liquid-water moist static energy ($s = C_p T + gz - L_v q_l$, where $C_p$ is the isobaric specific enthalpy, $T$ is the air temperature, $g$ is the gravitational acceleration, $z$ is the height above the surface, $L_v$ is the enthalpy of evaporation and $q_l$ is the liquid-water specific humidity) averaged over the depth $h$ of the well-mixed layer (which spans the region between the base of the cloud-top inversion and the top of the surface inversion, Figure 5d-f), $E$ is the entrainment velocity at cloud top, $\Delta s$ is the jump in $s$ across the cloud-level inversion, $\Delta F_{\text{rad}}$ is the net radiative divergence across the layer and $F_b$ is the turbulent heat flux across the bottom of the layer. Neglecting $F_b$, the ratio $\alpha = E\ \Delta s\ /\ \Delta F_{\text{rad}}$ therefore controls the rate at which the layer gains or loses energy: if $\alpha = 1$, $s$ will remain constant at its initial value, while $\alpha < 1$ implies cooling. Observational estimates in subtropical stratocumulus clouds indicate $\alpha$ is typically close to but somewhat smaller than 1 (Stevens 2006). Direct computation in our simulations (Table 1) shows that the same is true here, with $\alpha$ in the range 0.7–0.9 for the three simulations considered. Moreover, the values of *ds/dt* shown in Table 1 imply cooling rates around 0.5–2 K day$^{-1}$, consistently with the modest cooling of the temperature profiles after entry into the convective regime (Figure 5a-c). We do not compute $F_b$ explicitly, but its magnitude is estimated by the residual of the other terms of the equation, showing this term is generally much smaller than the other terms on the r.h.s. of (3).

| Experiment | $\frac{ds}{dt}$ | $\frac{E\Delta s}{h}$ | $-\frac{\Delta F_{rad}}{h}$ | $\alpha$ | Residual |
|---|---|---|---|---|---|
| T5Hi (24 – 52 h) | -0.003 | 0.09 | 0.10 | 0.9 | 0.007 |
| T5Lo (58 – 86 h) | -0.019 | 0.10 | 0.14 | 0.7 | 0.021 |
| T10Lo (92 – 120 h) | -0.024 | 0.10 | 0.14 | 0.7 | 0.016 |

Table 1. Values of the energetic tendency terms for the well-mixed sub-cloud layer in the convective regime, Equation (3) (J kg$^{-1}$ s$^{-1}$). All terms are averaged over a 28 hour time period after the onset of the convective regime in T5Hi, T5Lo, and T10Lo cases.

## 5. Surface energy balance and ice temperature evolution

With the insight into cloud evolution gained in the previous section, we can understand the main features of surface temperature and downward longwave evolution shown in Figure 3. First, Figure 3 shows that following an initial shock—in which the large initial imbalance between atmosphere and surface drives a large upward jump in surface temperature and downward longwave radiation—both $T_s$ and $F_{LWd}$ settle into a general long-term downward trend. This trend can be attributed to the fact that the cloud is rising throughout the simulations, cooling as it follows the initial dewpoint temperature profile (Figure 5d-f). This leads to decreasing longwave emission from the cloud, decreasing $F_{LWd}$ and cooling $T_s$. Cloud ascent is faster in T5Hi (because of the weaker cloud-top inversion, as discussed in Section 4) than in the other two simulations and thus the downward trend is stronger in that case.

Second, the downward trend discussed above is interrupted by upward jumps coinciding with the transition to the convective regime. As noted in Section 4.3, the cloud becomes thicker in the convective regime, leading to increased $F_{LWd}$. The different timing of these jumps is because the cloud must rise to some critical height above the surface before convection can set in, so the transition happens earlier the faster the cloud ascends.

Third, and most important, T5Hi has higher $F_{LWd}$ and $T_s$ than the two drier simulations through most of the 5-day duration. We attribute this difference to the higher cloud temperature (at given elevation) in the T5Hi case, due to its higher initial dewpoint temperature.

Another notable feature of the simulations is the persistent surface inversion seen in Figure 5d-f. Temperature profiles like those in Figure 5, with a shallow surface-based inversion overlayed by an elevated inversion, are commonly observed in the winter high Arctic (Tjernström and Graversen 2009; Zhang et al. 2022). The surface inversion matches the relatively cold surface temperature—controlled by the surface energy balance (1)—to the warmer air temperature aloft, which is separately controlled by the initial dewpoint temperature. Near-surface shear-produced turbulence transfers sensible heat down to the surface at a rate of around 5 W m$^{-2}$ on average (Figure 4j-l), with little difference among the three cases.

The conductive flux $F_C$ is initially negative in all three simulations (Figure 4j-l), implying energy flux downward from the surface into the snow layer, and explaining the initial warming of that layer (Figure 4m-o). $F_C$ becomes positive in the latter stages of the simulations: as the cloud rises, $F_{LWd}$ drops and $T_s$ cools, energy initially stored in the snow layer is returned to the atmosphere. The warming of the ice layers below the snow is limited in all cases. T5Hi shows a peak snow warming of around 13˚C, while the ice immediately below warms by only about 5˚C (Figure 4m). These results are quantitatively consistent with the observational results of Persson et al. (2017; their Fig. 6), providing confidence in our sea ice model. It appears that, given the thermal inertia and conductivity of the ice, the time scale of a single air-mass transformation process is simply too short to allow the deeper ice layers to respond; a rapid succession of similar events would be required to produce deeper effects in the ice, as found observationally by Persson et al. (2017).

## 6. Conclusions, discussion, and implications

We have studied the air-mass transformation process of an initially warm, cloud-free maritime air column in contact with initially cold sea ice under polar night conditions, using an atmospheric LES model coupled to a thermodynamic sea ice model in a set of simulations designed to test the sensitivity to initial air-mass temperature and humidity. We summarize our main results as follows:

1. For all initial temperature and humidity conditions considered, a mixed-phase cloud forms initially near the surface and then rises continuously at a rate of several hundred meters per day until it dissipates.
2. The cloud passes through two stages during its life cycle: an initial stable, drizzling stratus-like regime, followed by a convective stratocumulus-like regime.
3. The initially cold surface warms substantially over the course of the air-mass transformation process. Warming affects the topmost snow layer, but does not penetrate into the deeper sea ice layers; on the 5-day timescale considered, sea ice behaves as a thin slab of modest heat capacity.
4. Surface warming is due mostly to surface downward longwave radiation, which depends on the temperature and opacity of the cloud.
5. Cloud temperature is constrained to lie close to the initial dewpoint temperature at the same height—the cloud is always a few degrees colder than the initial dewpoint, but this offset changes little along the life cycle. Since the dewpoint depends only on humidity, memory of the initial temperature is lost.

The cloud evolution described in point 1 is broadly similar to that in an Arctic moist-intrusion event tracked with Lagrangian tracers in reanalysis data (You et al. 2022). It is also consistent with previous quasi-Lagrangian column-model studies (Wexler 1936, Herman and Goody 1976, Curry 1983, Cronin and Tziperman 2015, Pithan et al. 2016). In Curry (1983) convection is not represented and the simulations are permanently in the stable regime. Cronin and Tziperman (2015) show results for a case directly comparable to our T0RH80 case. Their results show that a mixed-phase cloud initially develops but collapses after only two days, while it persists for 5 days in our simulation. This difference could be due to differences in the treatment of dynamics (their model uses a convective parameterization) or microphysics, and would deserve closer study.

The overarching conclusion from our results is that surface warming over the air-mass transformation process modelled here is almost entirely controlled by initial air-mass humidity, regardless of initial temperature. The leading-order mechanism explaining this behavior is that initial humidity controls cloud temperature—via the dewpoint constraint—and cloud temperature controls longwave emission to the surface, which in turn controls surface temperature.

Taken at face value, this mechanism implies that surface warming during air-mass transformation should scale as initial dewpoint temperature. This is not the case, however: as shown by the solid line in Figure 2a, dewpoint temperature is an approximately logarithmic function of specific humidity (the inverse of the approximately exponential growth of saturation humidity with temperature dictated by the Clausius-Clapeyron relation). But surface warming actually increases roughly linearly with initial humidity. This happens because increasing humidity has additional effects which enhance surface warming above the dewpoint constraint. First, increasing humidity yields clouds with greater liquid water path and thus greater emissivity, enhancing downward longwave radiation particularly for the thin clouds of the stable regime.

Second, increasing humidity extends the total lifetime of the cloud, as is evident comparing Figures 4a and 4b. The mechanisms that terminate the cloud life cycle were examined in detail in a previous paper using a similar model framework (Dimitrelos et al. 2020). There, we found that the convective cloud dissipates when it ascends far enough that air entrained from above is too dry to balance moisture loss by ice crystal precipitation, leading to diminished cloud liquid water and a shutdown of convective destabilization by cloud-top radiative cooling. With a moister initial profile, the convective cloud can rise higher before it dissipates, lengthening the life cycle. The cloud spends more time in the convective regime, where surface effects are enhanced, leading to additional time-mean warming. These additional effects are less robust than the dewpoint constraint, and will depend on details of the microphysical processes—particularly cloud depletion by drizzle in the stable regime and by ice precipitation in the convective regime. It is therefore possible that the linear scaling of surface warming with humidity is a fortuitous result of the specific parameter choices and modelling assumptions made here, and other choices could lead to different scaling (which could be faster or slower than linear).

Nonetheless, taking the linear scaling found here at face value has an interesting implication for Arctic amplification (at least over persistent sea ice or land in winter). In a warming climate, marine air masses are expected to warm while maintaining roughly constant relative humidity, implying exponentially-increasing specific humidity following Clausius-Clapeyron scaling. The linear scaling then implies that sea ice or land subject to moist intrusions will also warm exponentially. We can quantify this effect by defining an amplification factor $A = \Delta T_s / \Delta T_{d0}$, where $\Delta T_{d0}$ and $\Delta T_s$ are the changes in surface dewpoint and surface temperature defined in the caption to Figure 2. We find $A = 1.2$ on average across the simulations. Since we expect marine air masses flowing into the poles to warm at roughly the same rate as sea surface temperature (SST) at their origin, and we note that dewpoint is linear in temperature assuming fixed relative humidity, a 1˚C warming of midlatitude/subpolar SST would give a typical 1.2˚C surface warming when the air masses move over sea ice or land. This is modest compared to the observed Arctic warming of ~2˚C per degree of midlatitude warming, but could be a contributing factor. If linear scaling continues to hold at higher temperatures, the effect would be larger and could be important in explaining warm winter continental interiors in warm paleoclimates (Cronin and Tziperman 2015).

Our results also have implications for the role of atmospheric energy transport in polar amplification. As noted in the Introduction, recent work indicates that changes in the moist component of polar MSE convergence have a much bigger impact on surface warming than changes in the dry component (Graversen and Burtu 2016, Yoshimori et al. 2017, Graversen and Langen 2019). Our results provide a potential explanation for this difference in the surface effects of dry versus moist energy transport: when air masses are advected into the polar region, memory of their original temperature is quickly lost by cloud-top radiation to space and plays little role in determining surface warming. We therefore expect changes in the dry component of MSE convergence to play a minor role in driving surface temperature change compared to the moist component.

To make the connection explicit, suppose our simulations represent a moist intrusion which enters a region of Arctic pack ice at time t=0 and exits at time t=5 days. The MSE convergence into the region by this moist intrusion event is [$h$(t=0) – $h$(t=5 days)] / (5 days), where $h$ is the column-integrated MSE content. We take the dry and moist contributions to MSE as $C_p\, T + gz$ and $L_v\, q$ respectively, where $T$ and $q$ are temperature and specific humidity and other symbols are defined as in Equation (3), and integrate from the surface to 3500 m. The results (Table 2) show that the initially warmer simulation T10Lo converges more MSE than the colder simulation T5Lo, but the two give almost exactly the same surface warming (Figure 2a). On the other hand, the initially moister simulation T5Hi converges *less* MSE than T5Lo, but produces surface warming that is around 5˚C *greater* (Figure 2a).

| | T5hi | T5lo | T10Lo | T5Hi–T5Lo | T10Lo–T5Lo |
|---|---|---|---|---|---|
| $C_p\, T + g\, z$ | 98 | 109 | 120 | –11 | 11 |
| $L_v\, q$ | 22 | 14 | 11 | 8 | –3 |
| $C_p\, T + g\, z + L_v\, q$ | 120 | 123 | 131 | –3 | 8 |

Table 2. Mean rate of vertically-integrated moist static energy convergence over the course of each simulation (first three columns), and differences between simulations (last two columns). All values are in W m$^{-2}$.

The climate implications sketched above are necessarily speculative at this point, and future work could explore whether the dewpoint constraint on cloud temperature found here can be identified in reanalysis products and climate models, for instance using Lagrangian tracers to link Arctic clouds to their maritime air masses of origin. It would also be of interest to extend the modelling framework to include a heterogeneous sea-ice model with multiple ice categories including open water, which would allow us to study the two-way interaction between clouds and sea ice (Kay and Gettelman 2009, Morrison et al. 2019). In addition, depletion of CCN by scavenging and precipitation could affect cloud opacity and lifetime, and it would be interesting to assess these effects by replacing our simple assumption of fixed CCN concentration with fully interactive aerosols.

*Acknowledgments.*

The computations were enabled by resources provided by the Swedish National Infrastructure for Computing (SNIC) at the National Supercomputer Centre (NSC) partially funded by the Swedish Research Council through grant agreement no. 2018-05973. This research has partly been supported by the Swedish Science Foundation (Vetenskapsrådet; grant no. 2015-05318) and the Knut and Alice Wallenberg Foundation (grant no. 2015.0162). We thank Matthew Shupe and Michael Tjernström for useful comments on the paper.

*Data availability statement.*

The data used in this study is uploaded at the website https://zenodo.org/ with assigned doi: 10.5281/zenodo.6347108. For questions about the model code, please contact annica@misu.su.se.

# APPENDIX

## Sea ice model

The sea ice model has four homogeneous layers of different density $\rho$, heat conductivity $k$, specific heat capacity $c$, and vertical extent $h$. The uppermost layer consists of snow. Below lies a thinner layer of snow which has a higher density and heat conductivity. This layer is named "snow ice" to distinguish it from the snow layer. The snow ice layer has the same specific heat as the layer of snow. Beneath the snow ice layer, two thick ice layers are placed which are distinct from each other due to their different densities and heat conductivities. The first layer is named "soft ice" and its density increases linearly downwards, whereas the opposite applies to its heat conductivity. The bottom layer is called "hard ice" and it has the same heat conductivity as the value at the bottom of the "soft ice" layer. The density, heat conductivity, specific heat, and thickness of snow (snow ice, "soft ice", "hard ice") are denoted as $\rho_s$ ($\rho_{si}$, $\rho_{soft}$, $\rho_{hard}$), $k_s$ ($k_{si}$, $k_{soft}$, $k_{hard}$), $c_s$ ($c_{si}$, $c_{soft}$, $c_{hard}$), and $h_s$ ($h_{si}$, $h_{soft}$, $h_{hard}$). The values of the aforementioned parameters are listed in Table A1. The surface roughness height is set to 0.0004 m, which reflects a flat snow-covered surface (Stull 1988).

The time evolution of temperature at layer midpoints and interfaces (9 levels in total, see Figure 1) is computed by integrating the following finite-difference energy transfer equations:

$$F_{LWd} - F_{LWu} + F_{SH} + F_{LH} + F_C + L = 0 \qquad \text{(A1)}$$

$$\rho_s c_s \frac{T_{snow}(t) - T_{snow}(t-dt)}{dt} = k_s \frac{T_{int1} - 2T_{snow} + T_s}{h_s^2} \qquad \text{(A2)}$$

$$k_s \frac{T_{int1} - T_{snow}}{\frac{h_s}{2}} = k_{si} \frac{T_{si} - T_{int1}}{\frac{h_{si}}{2}} \quad \text{(A3)}$$

$$\rho_{si} c_{si} \frac{T_{si}(t) - T_{si}(t-dt)}{dt} = k_{si} \frac{T_{int2} - 2T_{si} + T_{int1}}{h_{si}^2} \quad \text{(A4)}$$

$$k_{si} \frac{T_{int2} - T_{si}}{\frac{h_{si}}{2}} = k_{soft} \frac{T_{si} - T_{int2}}{\frac{h_{soft}}{2}} \quad \text{(A5)}$$

$$\rho_{soft2} c_{soft} \frac{T_{soft}(t) - T_{soft}(t-dt)}{dt} = k_{soft} \frac{T_{int3} - 2T_{soft} + T_{int2}}{h_{soft}^2} \quad \text{(A6)}$$

$$k_{soft} \frac{T_{int3} - T_{soft}}{\frac{h_{soft}}{2}} = k_{hard} \frac{T_{hard} - T_{int3}}{\frac{h_{hard}}{2}} \quad \text{(A7)}$$

$$\rho_{hard} c_{hard} \frac{T_{hard}(t) - T_{hard}(t-dt)}{dt} = k_{hard} \frac{T_{bot} - 2T_{hard} + T_{int3}}{h_{hard}^2} \quad \text{(A8)}$$

$$k_{hard} \frac{T_{bot} - T_{hard}}{\frac{h_{hard}}{2}} = F_W + \rho_{hard} L_f \frac{dh_{hard}}{dt} \quad \text{(A9)}$$

| Sea ice layer | Density (kg m$^{-3}$) | Heat conductivity (W m$^{-1}$ K$^{-1}$) | Specific heat (J kg$^{-1}$ K$^{-1}$) | Thickness (m) |
|---|---|---|---|---|
| snow | 350 | 0.31 | 2090 | 0.3 |
| snow ice | 600 | 0.5 | 2090 | 0.15 |
| soft ice (depth: 0.45 m) | 750 | 1 | 2108 | |
| soft ice (depth: 0.7 m) | 800 | 1.5 | 2108 | 0.5 |
| soft ice (depth 0.95) | 850 | 2 | 2108 | |
| hard ice | 900 | 2 | 2108 | 1.5 |

Table A1. Characteristics of sea ice model layers.

Here the temperatures in the middle of the snow, snow ice, soft, and hard ice layers are named $T_{snow}$, $T_{si}$, $T_{soft}$, $T_{hard}$, respectively. $T_s$ is the temperature at the surface while $T_{bot}$ is the temperature at the bottom of the sea ice, which is fixed at the freezing point of salt water (–2˚C). $T_{int1}$, $T_{int2}$, and $T_{int3}$ are the temperatures at the interfaces of the snow and the snow ice layer, snow ice and soft ice layers, and soft ice and hard ice layers, respectively. Time is indicated by $t$, and $dt$ =60 s is the time step. $F_W$ is the net flux of heat from the ocean to the sea ice bottom (Untersteiner et al. 1986) and is set to 2 W m$^{-2}$. $P_{soft2}$ is the density of the soft ice at 0.7 m depth. $F_{cbot}$ in Figure 1a is the term on the l.h.s of equation (A8).

The surface energy flux terms in Equation (A1) include the upward longwave radiative flux $F_{Lwu}=\varepsilon\sigma T_s^4$ , where $\varepsilon$ is the snow emissivity (0.92) and $\sigma$ is the Stefan-Boltzmann constant; the sensible and latent turbulent fluxes $F_{SH}=\rho_{\alpha}c_pC_su(T_a\text{-}T_s)$ and $F_{LH}=\rho_{\alpha}L_vC_eu(q_{\alpha}\text{-}q_s)$ respectively, where the bulk transfer coefficients $C_s$=1.2·10$^{-3}$ and $C_e$=0.55·10$^{-3}$ for sensible and latent heat, respectively (Thorpe et al. 1973) and the temperature and specific humidity at the surface and at 15 m altitude, denoted $T_s$, $q_s$ and $T_a$, $q_a$ respectively; the surface conductive heat flux $F_C=k_s(\partial T_{snow}/\partial z)_s \approx k_s(T_{snow}\text{-}\ T_s)/(h_s/2)$, and the latent heat involved in surface melting $L=\rho_sL_f(dH/dt)_s \approx \rho_sL_f(H(t)\text{-}H(t\text{-}dt))/dt$ where the total ice depth $H=h_s+h_{si}+h_{soft}+h_{hard}$. $L_v$ and $L_f$ are the latent heat of vaporization and fusion, respectively.

REFERENCES


Ali, S. M., and F. Pithan, 2020: Following moist intrusions into the Arctic using SHEBA observations in a Lagrangian perspective. *Quart. J. Roy. Meteorol. Soc*, **146**, 3522– 3533, https://doi.org/10.1002/qj.3859

Boeke, R. C., P. C. Taylor, and S. A. Sejas, 2021: On the nature of the Arctic’s positive lapse-rate feedback. *Geophys. Res. Lett*., **48**, e2020GL091 109.

Cardinale, C. J., and B. E. Rose, 2022: The Arctic surface heating efficiency of tropospheric energy flux events. *J. Climate*, **35**, https://doi.org/10.1175/JCLI–D–21–0852.1.

Cronin, T. W., and E. Tziperman, 2015: Low clouds suppress Arctic air formation and amplify high- latitude continental winter warming. *Proc. Nat. Acad. Sci. USA*, **112**, 11490–11495, https://doi.org/10.1073/pnas.1510937112.

Curry, J., 1983: On the formation of continental polar air. *J. Atmos. Sci.*, **40**, 2278–2292, https://doi.org/10.1175/1520-0469(1983)040<2278:OTFOCP>2.0.CO;2.

Dimitrelos, A., A. M. L. Ekman, R. Caballero, and J. Savre, 2020: A sensitivity study of Arctic air- mass transformation using large eddy simulation. *J. Geophys. Res. Atmos.*, **125**, e2019JD031738, https://doi.org/10.1029/2019JD031738.

Doyle, J., G. Lesins, C. Thackray, C. Perro, G. Nott, T. Duck, R. Damoah, and J. Drummond, 2011: Water vapor intrusions into the High Arctic during winter. *Geophys. Res. Lett.*, **38**, L12806, https://doi.org/10.1029/2011GL047493.

Feldl, N., S. Po-Chedley, H. K. Singh, S. Hay, and P. J. Kushner, 2020: Sea ice and atmospheric circulation shape the high-latitude lapse rate feedback. *npj Clim. Atmos. Sci.*, **3**, 1–9.

Forster, P., and Coauthors, 2021: The Earth's Energy Budget, Climate Feedbacks, and Climate Sensitivity, 923–1054. Cambridge University Press, Cambridge, United Kingdom and New York, NY, USA, https://doi.org/10.1017/9781009157896.009.

Fu, Q., and K.-N. Liou, 1993: Parameterization of the radiative properties of cirrus clouds, *J. Atmos. Sci*., **50**, 2008–2025, https://doi.org/10.1175/1520-0469(1993)050<2008:POTRPO>2.0.CO;2.

Garratt, J. R., 1994: *The Atmospheric Boundary Layer*, pp. 49–60, chap. 3.3, Cambridge University Press, Cambridge, U. K.

Gong, T., S. Feldstein, and S. Lee, 2017: The role of downward infrared radiation in the recent Arctic winter warming trend. *J. Climate*, **30**, 4937–4949, https://doi.org/10.1175/JCLI-D-16-0180.1.

Goosse, H., and Coauthors, 2018: Quantifying climate feedbacks in polar regions. *Nat. Commun.*, **9**, 1919, https://doi.org/10.1038/s41467-018-04173-0.

Graversen, R. G., and M. Burtu, 2016: Arctic amplification enhanced by latent energy transport of atmospheric planetary waves. *Quart. J. Roy. Meteorol. Soc*, **142**, 2046–2054, https://doi.org/10.1002/qj.2802.

Graversen, R. G., and P. L. Langen, 2019: On the role of the atmospheric energy transport in 2xCO2–induced polar amplification in CESM1. *J. Climate*, **32**, 3941–3956, https://doi.org/10.1175/JCLI-D-18-0546.1.

Hahn, L., K. C. Armour, D. S. Battisti, A. Donohoe, A. Pauling, and C. Bitz, 2020: Antarctic elevation drives hemispheric asymmetry in polar lapse-rate climatology and feedback. *Geophys. Res. Lett.*, **47**, e2020GL088965.

Hahn, L. C., K. C. Armour, M. D. Zelinka, C. M. Bitz, and A. Donohoe, 2021: Contributions to polar amplification in CMIP5 and CMIP6 models. *Front. Earth Sci.*, **9**, 710036.

Herman, G., and R. Goody, 1976: Formation and persistence of summertime Arctic stratus clouds. *J. Atmos. Sci*., **33**, 1537–1553.

Hwang, Y.-T., D. M. Frierson, and J. E. Kay, 2011: Coupling between Arctic feedbacks and changes in poleward energy transport. *Geophys. Res. Lett*., **38**, 17704.

Kay, J. E., and A. Gettelman, 2009: Cloud influence on and response to seasonal Arctic sea ice loss. *J. Geophys. Res. Atmos*., **114**, 18204.

Khvorostyanov, V. I., and J. Curry 2005: Fall velocities of hydrometeors in the atmosphere: Refinements to a continuous analytical power law, *J. Atmos. Sci*., **62**, 4343– 4357, https://doi.org/10.1175/JAS3622.1.

Klein, S. A., and Coauthors, 2009: Intercomparison of model simulations of mixed-phase clouds observed during the ARM Mixed-Phase Arctic Cloud Experiment. I: Single-layer cloud. *Quart. J. Roy. Meteor. Soc*., **135**, 979–1002, https://doi.org/https://doi.org/10.1002/qj.416.

Lawson, R. P., B. A. Baker, C. G. Schmitt, and T. Jensen, 2001: An overview of microphysical properties of Arctic clouds observed in May and July 1998 during FIRE ACE. *J. Geophys. Res. Atmos*., **106**, 14989–15014.

Lee, S., Gong, T., Feldstein, S. B., Screen, J. A., and Simmonds, I. (2017). Revisiting the cause of the 1989–2009 Arctic surface warming using the surface energy budget: Downward infrared radiation dominates the surface fluxes. *Geophys. Res. Lett.*, **44**, 10654–10661, https://doi.org/10.1002/2017GL075375

Liu, C., and E. A. Barnes, 2015: Extreme moisture transport into the Arctic linked to Rossby wave breaking. *J. Geophys. Res. Atmos*., **120**, 3774–3788.

Liu, Y., J. R. Key, S. Vavrus, and C. Woods, 2018: Time evolution of the cloud response to moisture intrusions into the Arctic during winter. *J. Climate*, **31**, 9389–9405.

Mauritsen, T., and Coauthors, 2011: An Arctic CCN-limited cloud-aerosol regime. *Atmos. Chem. Phys*., **11**, 165–173.

Mellado, J. P., 2017: Cloud-top entrainment in stratocumulus clouds. *Ann. Rev. Fluid Mech*., **49**, 145–169, https://doi.org/10.1146/annurev-fluid-010816-060231.

Messori, G., C. Woods, and R. Caballero, 2018: On the drivers of wintertime temperature extremes in the High Arctic. *J. Climate*, **31**, 1597–1618, https://doi.org/10.1175/JCLI-D-17-0386.1.

Middlemas, E., J. Kay, B. Medeiros, and E. Maroon, 2020: Quantifying the influence of cloud radiative feedbacks on Arctic surface warming using cloud locking in an earth system model. *Geophys. Res. Lett.*, **47**, e2020GL089207.

Morrison, H., and W. Grabowski 2008: Modeling supersaturation and subgrid-scale mixing with two-moment bulk warm microphysics, *J. Atmos. Sci.*, **65**, 792–812, https://doi.org/10.1175/2007JAS2374.1.

Morrison, H., and Coauthors, 2011: Intercomparison of cloud model simulations of Arctic mixed- phase boundary layer clouds observed during SHEBA/FIRE- ACE, *J. Adv. Model. Earth Syst.*, **3**, M06003, https://doi.org/10.1029/2011MS000066.

Morrison, H., G. de Boer, G. Feingold, J. Harrington, M. Shupe, and K. Sulia, 2012: Resilience of persistent Arctic mixed-phase clouds. *Nat. Geosci.*, **5**, 11–17, https://doi.org/10.1038/ngeo1332.

Morrison, A., J. E. Kay, W. Frey, H. Chepfer, and R. Guzman, 2019: Cloud response to Arctic sea ice loss and implications for future feedback in the CESM1 climate model. *J. Geophys. Res. Atmos.*, **124**, 1003–1020.

Park, D.-S. R., S. Lee, and S. B. Feldstein, 2015: Attribution of the recent winter sea ice decline over the Atlantic sector of the Arctic Ocean. *J. Climate*, **28**, 4027–4033, https://doi.org/10.1175/JCLI-D-15-0042.1.

Park, H.-S., S. Lee, S.-W. Son, S. B. Feldstein, and Y. Kosaka, 2015: The impact of poleward moisture and sensible heat flux on Arctic winter sea ice variability. *J. Climate*, **28**, 5030–5040, https://doi.org/10.1175/JCLI-D-15-0074.1.

Persson, P. O. G., M. D. Shupe, D. Perovich, and A. Solomon, 2017: Linking atmospheric synoptic transport, cloud phase, surface energy fluxes, and sea- ice growth: Observations of midwinter SHEBA conditions. *Clim. Dyn.*, **49**, 1341–1364, https://doi.org/10.1007/s00382- 016- 3383- 1.

Pithan, F., and T. Mauritsen, 2014: Arctic amplification dominated by temperature feedbacks in contemporary climate models. *Nat. Geosci.*, **7**, 181–184.

Pithan, F., B. Medeiros, and T. Mauritsen, 2014: Mixed- phase clouds cause climate model biases in Arctic wintertime temperature inversions. *Clim. Dyn*, **43**, 289–303, https://doi.org/10.1007/s00382- 013- 1964- 9.

Pithan, F., and Coauthors, 2016: Select strengths and biases of models in representing the Arctic winter boundary layer over sea ice: the Larcform 1 single column model intercomparison, *J. Adv. Model. Earth Syst.*, **8**, 1345–1357, https://doi.org/10.1002/2016MS000630.

Previdi, M., K. L. Smith, and L. M. Polvani, 2021: Arctic amplification of climate change: a review of underlying mechanisms. *Environ. Res. Lett.*, **16**, 093003, https://doi.org/10.1088/1748-9326/ac1c29.

Pruppacher, H. R., and J. D. Klett 1997: *Microphysics of Clouds and Precipitation*, 2nd ed., Kluwer Acad., Norwell, Mass.

Savre, J., A. M. L. Ekman, and G. Svensson, 2014: Technical note: Introduction to MIMICA, a large-eddy simulation solver for cloudy planetary boundary layers. *J. Adv. Model. Earth Syst.*, **6**, 630-649, https://doi.org/10.1002/2013MS000292.

Screen, J. A., and I. Simmonds, 2010: Increasing fall-winter energy loss from the Arctic Ocean and its role in Arctic temperature amplification. *Geophys. Res. Lett.*, **37**, L16 707.

Seifert, A., and K. Beheng, 2006: A two-moment cloud microphysics parameterization for mixed-phase clouds. Part 1: Model description. *Meteorol. Atmos. Phys.*, **92**, 45–66, https://doi.org/10.1007/s00703-005-0112-4.

Semmler, T., D. Jacob, K. H. Schlünzen, and R. Podzun, 2005: The water and energy budget of the Arctic atmosphere. *J. Climate*, **18**, 2515–2530.

Shupe, M. D., P. Kollias, P. O. G. Persson, and G. M. McFarquhar, 2008: Vertical motions in Arctic mixed-phase stratiform clouds. *J. Atmos. Sci.*, **65**, 1304–1322.

Shupe, M. D., P. O. G. Persson, I. M. Brooks, M. Tjernström, J. Sedlar, T. Mauritsen, S. Sjogren, and C. Leck, 2013: Cloud and boundary layer interactions over the Arctic sea ice in late summer, *Atmospheric Chem. Phys.*, **13**, 9379–9399, https://doi.org/10.5194/acp-13-9379-2013.

Silber, I., A. M. Fridlind, J. Verlinde, A. S. Ackerman, G. V. Cesana, and D. A. Knopf, 2021: The prevalence of precipitation from polar supercooled clouds. *Atmos. Chem. Phys*., **21**, 3949–3971.

Sokolowsky, G. A., and Coauthors, 2020: Contributions to the surface downwelling longwave irradiance during Arctic winter at Utqiaġvik (barrow), Alaska. *J. Climate*, **33**, 4555–4577.

Solomon, A., M. D. Shupe, P. O. G. Persson, and H. Morrison, 2011: Moisture and dynamical interactions maintaining decoupled Arctic mixed-phase stratocumulus in the presence of a humidity inversion, *Atmospheric Chem. Phys.*, **11**, 10127–10148, https://doi.org/10.5194/acp-11-10127-2011.

Sotiropoulou, G., and Coauthors, 2016: Atmospheric conditions during the Arctic Clouds in Summer Experiment (ACSE): Contrasting open water and sea ice surfaces during melt and freeze-up seasons. *J. Climate*, **29**, 8721–8744, https://doi.org/10.1175/JCLI-D-16-0211.1.

Stevens, B., 2006: Bulk boundary-layer concepts for simplified models of tropical dynamics. *Theor. Comput. Fluid Dyn.*, **20**, 279–304, https://doi.org/10.1007/s00162-006-0032-z.

Stuecker, M. F., and Coauthors, 2018: Polar amplification dominated by local forcing and feedbacks. *Nat. Clim. Change*, **8**, 1076–1081

Svensson, G., and T. Mauritsen, 2020: Arctic cloud systems. *Clouds and Climate: Climate Science's Greatest Challenge,* Cambridge University Press.

Taylor, P. C., and Coauthors, 2022: Process drivers, inter-model spread, and the path forward: A review of amplified Arctic warming. *Front. Earth Sci*., **9**, 758361, https://doi.org/10.3389/feart. 2021.758361.

Thorpe, S.A, 1973: Turbulence in stably stratified fluids: A review of laboratory experiments. *Bound.-Layer Meteorol.*, **5**, 95–119, https://doi.org/10.1007/BF02188314.

Tjernström, M., 2007: Is there a diurnal cycle in the summer cloud-capped arctic boundary layer? *J. Atmos. Sci*., **64**, 3970–3986.

Tjernström, M., and R. G. Graversen, 2009: The vertical structure of the lower Arctic troposphere analysed from observations and the ERA-40 reanalysis. *Quart. J. Roy. Meteor. Soc*., **135**, 431– 443.

Verlinde, J., and Coauthors, 2007: The mixed-phase Arctic cloud experiment. *Bull. Am. Meteorol. Soc.*, **88**, 205–222.

Wendisch, M., and Coauthors, 2019: The Arctic cloud puzzle: Using ACLOUD/PASCAL multi- platform observations to unravel the role of clouds and aerosol particles in Arctic amplification. *Bull. Am. Meteorol. Soc.*, **100**, 841–871.

Wexler, H., 1936: Cooling in the lower atmosphere and the structure of polar continental air. *Mon. Wea. Rev*, **64**, 122–136, https://doi.org/10.1175/1520-0493(1936)64<122:CITLAA>2.0.CO;2.

Woods, C., R. Caballero, and G. Svensson, 2013: Large-scale circulation associated with moisture intrusions into the Arctic during winter. *Geophys. Res. Lett.*, **40**, 4717–4721, https://doi.org/10.1002/grl.50912.

Woods, C., and R. Caballero, 2016: The role of moist intrusions in winter Arctic warming and sea ice decline. *J. Climate*, **29**, 4473–4485, https://doi.org/10.1175/JCLI-D-15-0773.1.

Yoshimori, M., A. Abe-Ouchi, and A. Laîné, 2017: The role of atmospheric heat transport and regional feedbacks in the arctic warming at equilibrium. *Clim. Dyn.*, **49**, 3457–3472.

You, C., M. Tjernström, and A. Devasthale, 2022: Warm and moist air intrusions into the winter Arctic: a Lagrangian view on the near-surface energy budgets. *Atmos. Chem. Phys.*, **22**, 8037– 8057.

Zhang, Y., B. Zhang, and N. Yang, 2022: Characteristics of temperature and humidity inversions based on high-resolution radiosonde observations at three Arctic stations. *J. Appl. Meteor. Clim.*, **61**, 415–428.